REPORT

QUANTUM OPTICS

Quantum interface of an electron and a nuclear ensemble

D. A. Gangloff[1]*†, G. Éthier-Majcher[1]*‡, C. Lang[1], E. V. Denning[1,2], J. H. Bodey[1], D. M. Jackson[1], E. Clarke[3], M. Hugues[4], C. Le Gall[1], M. Atatüre[1]†

Coherent excitation of an ensemble of quantum objects underpins quantum many-body phenomena and offers the opportunity to realize a memory that stores quantum information. Thus far, a deterministic and coherent interface between a spin qubit and such an ensemble has remained elusive. In this study, we first used an electron to cool the mesoscopic nuclear spin ensemble of a semiconductor quantum dot to the nuclear sideband–resolved regime. We then implemented an all-optical approach to access individual quantized electronic-nuclear spin transitions. Lastly, we performed coherent optical rotations of a single collective nuclear spin excitation—a spin wave. These results constitute the building blocks of a dedicated local memory per quantum-dot spin qubit and promise a solid-state platform for quantum-state engineering of isolated many-body systems.

A controllable quantum system provides a versatile interface to observe and manipulate the quantum properties of an isolated many-body system (*1*). In turn, collective excitations of this ensemble can store quantum information as a memory (*2*, *3*)—a contemporary challenge for quantum technologies. Whereas a number of hybrid qubit-ensemble approaches have been pursued in the last decade (*4*, *5*), nuclear spins remain the most promising ensemble candidate because of their unparalleled coherence times. Such a nuclear ensemble interfaced with a (spin) qubit is described elegantly by the central spin model (*6*, *7*), studied in donor atoms embedded in Si (*8*, *9*), diamond color centers (*10*–*12*), and semiconductor nanostructures (*13*–*16*). In these systems, the states of the central spin and of the spin ensemble that surrounds it are tied by mutual interaction, allowing proxy control over the many-body system and long-lived storage in principle (*2*). Realizing this scenario with an electron in a semiconductor quantum dot (QD) offers access to a large ensemble of nuclear spins with quasi-uniform coupling to the central spin. In this system, coherent addressing of the ensemble via the central spin has yet to be shown, and a limiting factor is the thermal fluctuations of the surrounding spins that obfuscate the state-selective transitions required for such control. However, driving the central spin can stimulate the exchange of energy with the surrounding spins and thus modify the properties of the central spin's environment. This has been shown to reduce the uncertainty on the collective spin state of the isolated QD nuclei, leading to prolonged electron spin coherence (*17*–*21*).

In this Report, we use all-optical stimulated Raman transitions to manipulate the electron-nuclear system and realize a coherent interface. First using a configuration analogous to Raman cooling of atoms (*22*), we drive the electron spin to reduce the thermal fluctuations of the nuclear spin ensemble (Fig. 1A). Cooling of the nuclear spin fluctuations to an effective temperature well below the nuclear Zeeman energy (<1 mK), followed immediately by detuned probing of the electron spin resonance (ESR), allows us to reveal an excitation spectrum of transitions between many-body states that are collectively enhanced by the creation of a single nuclear spin–wave excitation—a nuclear magnon. Lastly, we drive a single magnon transition resonantly, inducing coherent exchange between the electron spin and the nuclear spin ensemble.

Our system consists of a charge-controlled semiconductor QD (*23*), where a single electron spin is coupled optically to a charged exciton state and magnetically to an isolated reservoir of N (10^4 to 10^5) nuclear spins of As (total spin $I = 3/2$), Ga ($I = 3/2$), and In ($I = 9/2$), as in Fig. 1B. We drive the electron-nuclear system with a narrow two-photon resonance at detuning δ from an excited state, whose linewidth Γ is tunable via the optical pumping rate of the electron spin (Fig. 1B), as with Raman cooling (*22*). The optical parameters set the dissipation rate relative to the energy scales relevant for cooling, which are the nuclear Zeeman energy ω_n and the hyperfine coupling energy per nucleus A_c, like the phonon and photon recoil energies for trapped atoms (*22*).

In atomic physics, the motion of an atom relative to detuned driving fields leads to a velocity-dependent absorption rate via the Doppler effect and, together with the photon recoil momentum, to a damping force that is the basis of laser cooling of atomic motion (*24*). In our system, the hyperfine interaction between the electron and nuclei leads to a shift of the ESR that depends linearly on the net polarization I_z of the nuclei (*6*); this Overhauser shift $2A_cI_z$ thus leads to a polarization-dependent absorption rate. In the presence of material strain, the hyperfine interaction enables optically driven nuclear spin flips that can be modeled as sidebands of amplitude $\eta\Omega$ ($\eta < 1$) on a principal transition of amplitude Ω that flips the electron spin only (*25*, *26*). With fast electron spin reset, absorption on the sidebands at polarization-dependent rates $W_\pm(I_z)$ can increase (+) or decrease (–) the mean nuclear polarization I_z, as shown in Fig. 1C, in a process known as dynamic nuclear polarization (*6*, *27*). The evolution of this complex system pitting drift $W_\pm$ against diffusion $\Gamma_d(I_z)$ is captured elegantly by a simple rate equation (*26*, *28*):

$$\frac{dI_z}{dt} = -\frac{\Gamma_{\rm tot}}{(3N/2)}\left[I_z - f(I_z)\right] \qquad (1)$$

where $\Gamma_{\rm tot} = W_+ + W_- + \Gamma_d$ is the total diffusion rate and $f(I_z) = (3N/2)(W_+ - W_-)/\Gamma_{\rm tot}$ is the cooling function that reduces fluctuations, as in Doppler cooling (*24*). The polarization $I_0 = \delta/(2A_c)$ is the steady state of the dynamical system defined by Eq. 1, as shown in Fig. 1C. Rate extrema occur when the Overhauser shift brings a sideband transition in resonance with the drive, $|2A_c(I_z - I_0)| \approx \omega_n$ (for $\omega_n \gg A_c$), suggesting that Overhauser fluctuations can be reduced below the nuclear Zeeman energy, ω_n. The driven ensemble experiences damping proportional to the cooling-function gradient, $(5/3)f'(I_0)$. For a probability distribution $p(I_z)$, the fluctuations ΔI_z^2 are reduced from their thermal-equilibrium value $5N/4$ (Fig. 1C) by (*23*, *28*)

$$\frac{\Delta I_z^2}{5N/4} = \frac{1-\left(\frac{2}{5N}I_0\right)^2}{1-\frac{5}{3}f'(I_0)} \qquad (2)$$

From the electron's perspective, a commensurate reduction of fluctuations occurs for a highly polarized nuclear ensemble, which to date has not been achieved. This occurs at thermal equilibrium when the energy k_BT (where k_B is the Boltzmann constant and T is temperature) falls below the system's defining energy scale, here the nuclear Zeeman energy $\hbar\omega_n$ (where $\hbar$ is Planck's constant). The fluctuations in Fig. 1C thus correspond to an effective temperature below $T = \hbar\omega_n/k_B = 1$ mK (*23*).

Figure 2 highlights the optimal conditions for cooling the nuclear ensemble. The electron coherence time T_2^* is a direct measure of nuclear polarization fluctuations $\Delta I_z^2 = 1/2(A_cT_2^*)^2$ (*21*, *23*); therefore, Ramsey interferometry on the electron spin (*29*, *30*) serves as our thermometer. We

---

[1]Cavendish Laboratory, University of Cambridge, JJ Thomson Avenue, Cambridge CB3 0HE, UK. [2]Department of Photonics Engineering, Technical University of Denmark, 2800 Kgs. Lyngby, Denmark. [3]EPSRC National Epitaxy Facility, University of Sheffield, Broad Lane, Sheffield S3 7HQ, UK. [4]Université Côte d'Azur, CNRS, CRHEA, rue Bernard Gregory, 06560 Valbonne, France.
*These authors contributed equally to this work.
†Corresponding author. Email: dag50@cam.ac.uk (D.A.G.); ma424@cam.ac.uk (M.A.) ‡Present address: Anyon Systems, 1985 55e Avenue #100, Dorval, QC H9P 1G9, Canada.

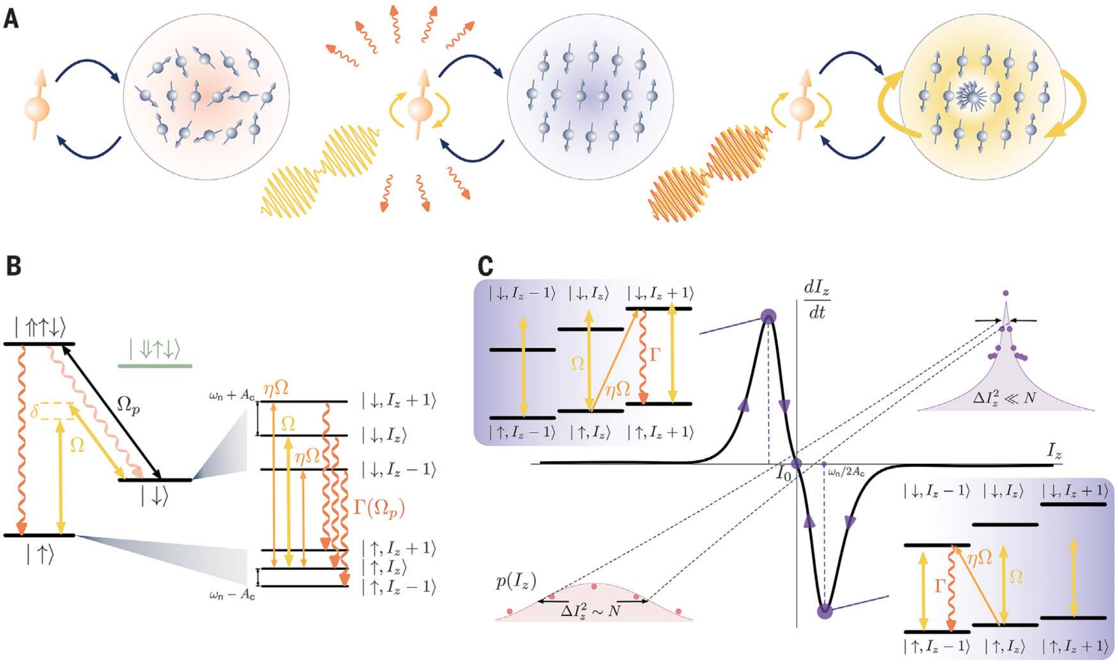

Fig. 1. An electron controls a nuclear ensemble. (**A**) The central spin scenario. (Left) A spin interacts with a thermally fluctuating ensemble; (middle) in the presence of dissipation, the driven spin can cool the ensemble to a lower effective temperature; (right) driving the spin can create coherent superpositions of single spin flips as collective excitations of the cooled ensemble. (**B**) Realization of this scenario in a semiconductor QD, under a magnetic field in Voigt geometry, optically pumped to electronic spin state $|\uparrow\rangle$ by a resonant drive Ω_p via the trion state $|\Uparrow\uparrow\downarrow\rangle$ of homogeneous linewidth Γ_0 = 150 MHz at a rate $\Gamma \sim \Omega_p^2/4\Gamma_0 \leq 38$ MHz. The electron spin splitting is (Overhauser) shifted by its hyperfine interaction $2A_cI_z$, where A_c = 600 kHz, with an ensemble of N (10^4 to 10^5) nuclear spins, described by mean polarization states $I_z = [-3N/2, 3N/2]$ (taken for spin 3/2). Far-detuned (≳1-nm) Raman beams drive the ESR at a Rabi frequency $\Omega \lesssim 40$ MHz, including transitions that simultaneously flip a single nuclear spin $I_z \rightarrow I_z \pm 1$ at frequency $\eta\Omega$ ($\eta < 1$). (**C**) Cooling dynamics. The time derivative of polarization dI_z/dt depends on the polarization I_z, through the Overhauser shift and the nuclear spin flipping transitions $W_\pm$. The polarization I_0 is the dynamical system's stable point, where the width ΔI_z^2 of the probability distribution $p(I_z)$ is reduced (violet) compared with its value without cooling (red).

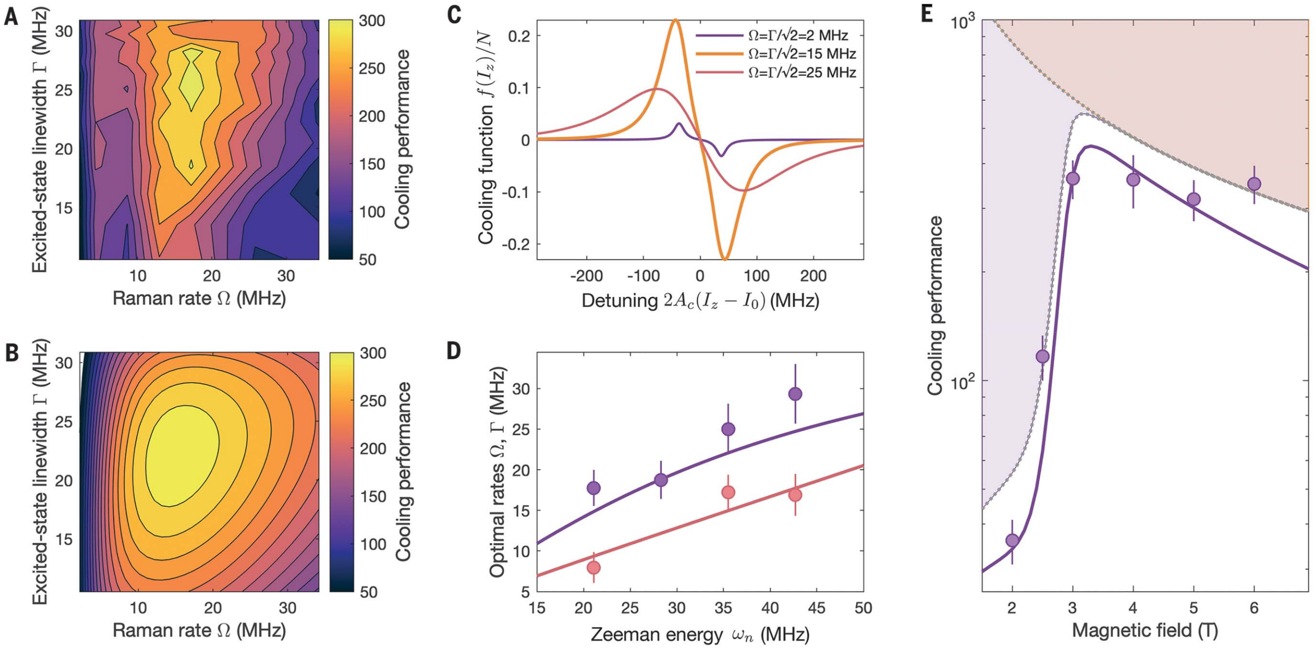

Fig. 2. Optimal cooling of the nuclear ensemble. (**A**) Experimental Raman cooling performance $5N/4\Delta I_z^2$ as a function of Raman rate Ω and excited-state linewidth Γ at 5 T. The maximum of 300 is reached for $\Omega \sim \omega_n/2$ and saturation conditions $\Gamma \sim \sqrt{2}\Omega$. (**B**) Theoretical prediction of (A). (**C**) Calculated cooling curves $f(I_z) \propto W_+ - W_-$ at optical saturation $\Omega = \Gamma/\sqrt{2}$ for increasing rates. The largest damping $f'(I_0)$ occurs when $\Omega \sim \omega_n/2$ = 18 MHz (orange curve). (**D**) Raman rate and excited-state linewidth at the measured optimal cooling performance as a function of ω_n at 3, 4, 5, and 6 T. Solid curves are the corresponding theoretical calculations. (**E**) Magnetic-field optimal cooling. Circles represent the maximum cooling performance at a given magnetic field. Shaded regions are cooling limits, and curves are from a theoretical model [see main text and (*23*)]. Error bars represent one standard deviation of uncertainty.

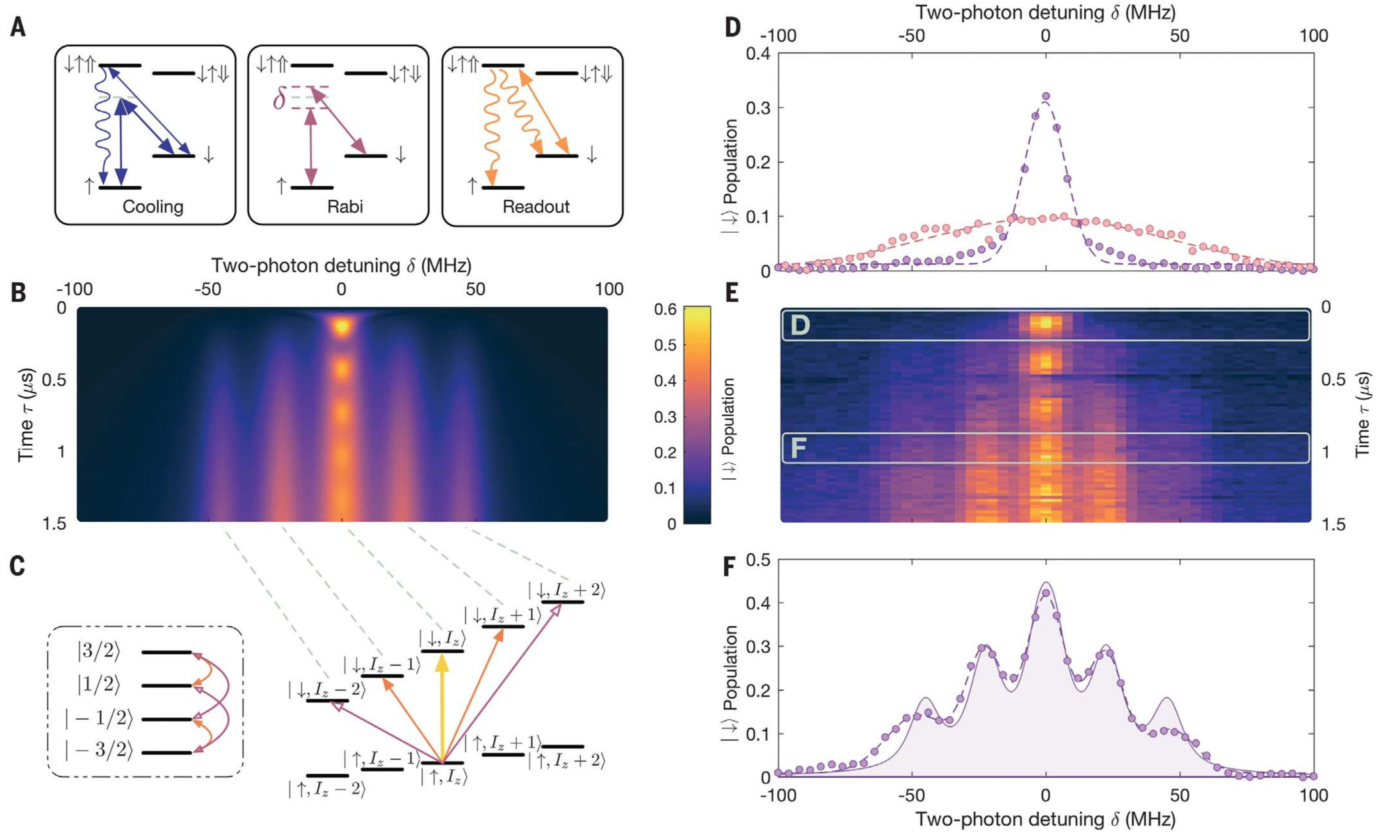

Fig. 3. Resolving single nuclear magnons. (**A**) Spectrum measurement sequence. (Left to right) Raman cooling, Rabi drive ESR at detuning δ for time τ, and optical readout of the electron |↓⟩ population (*23*). (**B**) Theoretical ESR spectrum buildup as a function of two-photon detuning δ and drive time τ for a Rabi frequency of Ω = 3.3 MHz on the central transition. Sideband coupling η is fitted (*23*). The model is a master-equation treatment of the driven electron-nuclear system, accounting for electron dephasing, where the nuclear system is reduced to collective states with polarization close to I_0 (*23*). (**C**) (Right) The ladder of electronic and nuclear states showing the carrier $I_z \rightarrow I_z$ and sideband transitions $I_z \rightarrow I_z \pm 1$, $I_z \pm 2$ from an initially spin-up polarized electron at a nuclear polarization of I_z. (Left) The same transitions represented within a single nuclear spin-3/2 manifold. (**D**) Spectra with optimal (violet) and poor (red) Raman cooling at average delay τ = 0 – 150 ns. The dashed curves are Gaussian fits with standard deviations of 7.7 and 44.6 MHz, respectively. (**E**) Experimental spectrum buildup with Ω = 3.8 MHz. (**F**) Spectrum at integrated delay τ = 850 – 1000 ns. The solid curve is the same time slice averaged from the theory spectrum of (B). The dashed curve is five Gaussian functions centered at δ ~ 0, ±ω_n, ±2ω_n (*23*).

parametrize temperature as a cooling performance factor, $(5N/4)/\Delta I_z^2$, as a function of Raman rate Ω and excited-state linewidth Γ, as shown in Fig. 2A. A maximum of ~300 is found where the Raman rate Ω = 17 MHz is approximately half of the nuclear Zeeman energy (as a linear frequency), ω_n = 36 MHz, and the excited-state linewidth corresponds to optical saturation, Γ ~ 25 MHz. This is in quantitative agreement with our theoretical prediction, shown in Fig. 2B, that accounts for nuclear spin diffusion and inhomogeneous broadening (*23*).

The Raman rate Ω and the electronic excited-state linewidth Γ determine the spectral selectivity and the diffusion rate of the cooling process. For best cooling, no absorption should occur at the stable point I_0, whereas sideband absorption should turn on sharply in response to polarization fluctuations away from I_0. Optimal values for Ω and Γ thus depend on the sideband spacing ω_n: $\Omega, \Gamma \ll \omega_n$ entails high spectral selectivity but weak sideband absorption near I_0, whereas $\Omega, \Gamma \sim \omega_n$ entails strong absorption on the sidebands but low spectral selectivity. Figure 2C depicts this dependence of the cooling function $f(I_z)$ on the optical parameters: The damping $f'(I_0)$ is largest when the Raman rate is approximately half of the nuclear Zeeman energy, $\Omega \sim \omega_n/2$, and when the Raman rate is close to saturation, $\Omega \sim \Gamma/\sqrt{2}$. We confirm this experimentally in Fig. 2D by changing the applied magnetic field: The values of Ω and Γ that optimize the cooling performance are proportional to the sideband spacing.

The lowest temperature of our system is a function of distinct diffusion and broadening processes competing with Raman cooling through magnetic field–dependent rates: In the low-field regime, homogeneous broadening of the ESR dominates (*29*, *30*) (purple region in Fig. 2E), whereas in the high-field regime, optical diffusion does (*23*) (red region in Fig. 2E). Further, electron-mediated nuclear spin diffusion (*31*, *32*) counteracts Raman cooling in both regimes. Figure 2E displays the magnetic field dependence of the temperature optimized against optical parameters. Our results follow closely the field-dependent bounds obtained from modeling the diffusion processes (solid curve) and establish the globally optimal cooling performance of ~400 at ~3.3 T. Operating close to this field, we prepare the nuclear ensemble at an effective temperature of 200 μK (*23*). There, the Overhauser fluctuations are well below the nuclear Zeeman energy, $2A_c\sqrt{\Delta I_z^2}$ = 7 MHz < ω_n = 22 MHz (at 3 T), which places our system well into the sideband-resolved regime.

We now probe the electron spin state in the coherent regime where dissipation is turned off, Γ → 0. We drive the ESR for a time τ at a detuning δ and measure the electron |↓⟩ population (Fig. 3A). Figure 3B shows this time-resolved spectrum obtained from our theoretical analysis (*23*), where we expect five distinct processes, as shown in Fig. 3C: a central transition at δ = 0 and four sideband transitions at δ = ±ω_n, ±2ω_n. The nuclear spin-flip transitions originate from the strain-induced electric field gradient that couples to the quadrupole moment of all QD nuclei, mixing their Zeeman eigenstates (*16*). The quadratic nature of this interaction allows the nuclear polarization to change either by one quantum ($I_z \rightarrow I_z \pm 1$) (*25*, *26*) or by two quanta ($I_z \rightarrow I_z \pm 2$); these selection rules apply to all QD nuclear spin species. A first-order perturbative expansion of the hyperfine interaction (*23*) dresses the ESR with these transitions. When the driving field with amplitude Ω is detuned from the principal transition by one or two units of nuclear Zeeman energy ω_n, these resonant transitions occur with amplitude ηΩ, as sidebands of strength $\eta = \mathcal{D}A_{nc}/\omega_n$; here, $A_{nc} \approx 0.015A_c$ is the noncolinear hyperfine constant parametrizing the perturbation. The driven electron cannot distinguish the ~N possible spin flips that take I_z to $I_z \pm 1, \pm 2$, which leads to the degeneracy factor $\mathcal{D} \sim \sqrt{N}$. This underpins the collective enhancement (*33*) that makes the nuclear spin-flip sideband transitions so prominent in our system.

Figure 3D shows the experimental spectra averaged over short delays τ = 0 – 150 ns, where Ωτ ~ π, revealing the principal ESR with optimal (violet data) and suboptimal (red data) cooling. The feature width is a convolution of the drive Rabi frequency Ω with the Overhauser field fluctuations $2A_c\sqrt{\Delta I_z^2}$ and highlights the spectral narrowing achieved by Raman cooling. Figure 3E shows the time-frequency map of this measurement. At δ = 0, the principal ESR leads to Rabi oscillations at Ω = 3.8 MHz. At larger delays where ηΩτ ~ π and at a sufficient detuning from the principal transition δ ≫ Ω, the emergence of four sideband processes agrees well with our predictions. Figure 3F is a standout observation of the sideband spectrum, integrated over τ = 850 – 1000 ns. A five-Gaussian fit (dashed curve) verifies that the sidebands emerge at integer multiples of ω_n, and the shaded area highlights the theoretical spectrum. Our results confirm that the sideband drive can excite selectively a single nuclear spin flip in the ensemble and show that ~N sufficiently identical nuclei are simultaneously coupled to the driven electron. In contrast to magnons in ferromagnetic materials, this type of collective excitation is based on an electron-mediated interaction, in close analogy to photon-mediated magnon-polariton modes in strongly coupled light-matter interfaces (*3*). Until now, such a collective nuclear spin excitation had been observed only as ensemble measurements of atomic gases (*34*) and magnetic materials (*35*, *36*), whereas our result represents the deterministic generation of a single nuclear magnon by interfacing the nuclei with an elementary controllable quantum system.

This spectral selectivity enables coherent generation of a single-spin excitation, provided it is faster than the dephasing times of the electron ($T_2 \approx 1$ μs) (*30*) and the nuclei ($T_2 \approx 10$ μs) (*32*). Figure 4 illustrates this coherent drive via Rabi oscillations. Detuning maximally from the quenching effect of coupling to the principal transition, we drive one of the second sidebands ($I_z \rightarrow I_z + 2$) with $\eta\Omega > 1/T_2$ (Fig. 3C) and measure for delays $\tau \gtrsim \pi/\eta\Omega$. Figure 4 presents measurements with three Rabi frequencies, Ω = 7, 9, and 12 MHz (*23*). Oscillations of the electron spin population at a fraction η of the carrier frequency Ω are a direct measurement of coherent electron-nuclear dynamics. We attribute the sharp appearance of oscillations above a Rabi frequency Ω ~ 10 MHz to reaching a sufficient sideband coupling ηΩ ~ 1.5 MHz to overcome inhomogeneities, which exist on a megahertz scale within a more strongly coupled subset of nuclei (*23*). Our master-equation model (solid lines in Fig. 4) captures this inhomogeneous broadening that limits the Rabi oscillations. The gray-shaded areas represent ±20% deviations of Rabi frequency, and our data's drift toward lower Rabi frequency at long delays suggests a dephasing mechanism that depends on accumulated phase Ωτ. Our model further allows us to reconstruct the nuclear spin population transfer, where the effect of off-resonant excitation of the principal transition is not present, and shows that the electron spin population transfer is accompanied predominantly by nuclear spin population transfer (*23*).

The value η ~ 15%, directly extracted from the coherent oscillations in Fig. 4, confirms the ~$\sqrt{N}$ enhancement of the sideband transition strength arising from the collective nature of the magnon excitation. With sufficient coupling homogeneity, the nuclei can be treated as an ensemble of N = 30,000 indistinguishable spins under the hyperfine interaction with the electron. Oscillations in Fig. 4 indicate the creation and retrieval of a coherent superposition of a single nuclear spin excitation among all spins, forming the basis of many-body entanglement as found for Dicke states (*33*). This occurs despite operating near-zero polarization, where the degeneracy of nuclear states is maximal. This exchange of coherence is far from the bosonic approximation available for a fully polarized ensemble (*2*). Furthermore, an intermediate drive time ηΩτ = π/2 generates an inseparable coherent superposition state for the electron and the nuclei.

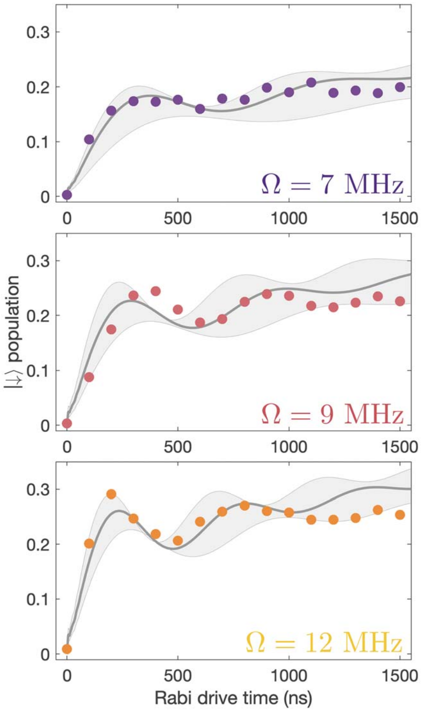

Fig. 4. Coherent oscillations of a nuclear magnon. Electronic excited-state |↓⟩ population (*23*), measured after a Rabi pulse of τ at δ = $-2\omega_n$ = 52 MHz detuning, at 3.5 T. The carrier Rabi frequency Ω is 7, 9, and 12 MHz (*23*) for measurements shown in the top, middle, and bottom panels, respectively. Solid curves are the corresponding theoretical calculations with η = 15% for the same carrier Rabi frequencies. The shaded areas represent a ~±20% deviation in model Rabi frequency.

In this work, we have realized a coherent quantum interface between a single electron and 30,000 nuclei by using light. By making use of the back action of a single nuclear spin flip on the electron, the development of a dedicated quantum memory per electron spin qubit in semiconductor QDs becomes viable. Future possibilities also include creating and monitoring tailored collective quantum states of the nuclear ensemble, such as Schrödinger cat states, by harnessing Hamiltonian engineering techniques.

REFERENCES AND NOTES

1. L. Amico, R. Fazio, A. Osterloh, V. Vedral, *Rev. Mod. Phys.* **80**, 517–576 (2008).
2. J. M. Taylor, C. M. Marcus, M. D. Lukin, *Phys. Rev. Lett.* **90**, 206803 (2003).
3. K. S. Choi, A. Goban, S. B. Papp, S. J. van Enk, H. J. Kimble, *Nature* **468**, 412–416 (2010).
4. X. Zhu *et al.*, *Nature* **478**, 221–224 (2011).
5. Y. Tabuchi *et al.*, *Science* **349**, 405–408 (2015).
6. A. Abragam, L. C. Hebel, *Am. J. Phys.* **29**, 860–861 (1961).
7. D. Stanek, C. Raas, G. S. Uhrig, *Phys. Rev. B* **90**, 064301 (2014).
8. R. de Sousa, S. Das Sarma, *Phys. Rev. B* **68**, 115322 (2003).
9. J. J. Pla *et al.*, *Nature* **489**, 541–545 (2012).
10. L. Childress *et al.*, *Science* **314**, 281–285 (2006).
11. G. Balasubramanian *et al.*, *Nat. Mater.* **8**, 383–387 (2009).
12. N. Kalb *et al.*, *Science* **356**, 928–932 (2017).
13. A. V. Khaetskii, D. Loss, L. Glazman, *Phys. Rev. Lett.* **88**, 186802 (2002).
14. I. A. Merkulov, A. L. Efros, M. Rosen, *Phys. Rev. B* **65**, 205309 (2002).
15. H. Bluhm *et al.*, *Nat. Phys.* **7**, 109–113 (2011).
16. B. Urbaszek *et al.*, *Rev. Mod. Phys.* **85**, 79–133 (2013).
17. D. Stepanenko, G. Burkard, G. Giedke, A. Imamoglu, *Phys. Rev. Lett.* **96**, 136401 (2006).
18. A. Greilich *et al.*, *Science* **317**, 1896–1899 (2007).
19. D. J. Reilly *et al.*, *Science* **321**, 817–821 (2008).
20. X. Xu *et al.*, *Nature* **459**, 1105–1109 (2009).
21. G. Éthier-Majcher *et al.*, *Phys. Rev. Lett.* **119**, 130503 (2017).
22. D. J. Heinzen, D. J. Wineland, *Phys. Rev. A* **42**, 2977–2994 (1990).
23. Supplementary materials.
24. W. D. Phillips, *Rev. Mod. Phys.* **70**, 721–741 (1998).
25. C.-W. Huang, X. Hu, *Phys. Rev. B* **81**, 205304 (2010).
26. A. Högele *et al.*, *Phys. Rev. Lett.* **108**, 197403 (2012).
27. B. Eble *et al.*, *Phys. Rev. B* **74**, 081306 (2006).
28. W. Yang, L. J. Sham, *Phys. Rev. B* **88**, 235304 (2013).
29. A. Bechtold *et al.*, *Nat. Phys.* **11**, 1005–1008 (2015).
30. R. Stockill *et al.*, *Nat. Commun.* **7**, 12745 (2016).
31. C. Latta, A. Srivastava, A. Imamoğlu, *Phys. Rev. Lett.* **107**, 167401 (2011).
32. G. Wüst *et al.*, *Nat. Nanotechnol.* **11**, 885–889 (2016).
33. R. H. Dicke, *Phys. Rev.* **93**, 99–110 (1954).
34. B. R. Johnson *et al.*, *Phys. Rev. Lett.* **52**, 1508–1511 (1984).
35. G. Seewald, E. Hagn, E. Zech, *Phys. Rev. Lett.* **78**, 5002–5005 (1997).

36. L. V. Abdurakhimov, Y. M. Bunkov, D. Konstantinov, *Phys. Rev. Lett.* **114**, 226402 (2015).

ACKNOWLEDGMENTS

We thank A. Nunnenkamp and G. Burkard for critical reading of the manuscript and R. Stockill for helpful discussions. **Funding:** This work was supported by ERC PHOENICS (617985) and EPSRC NQIT (EP/M013243/1). Sample growth was carried out in the EPSRC National Epitaxy Facility. D.A.G. acknowledges a St. John's College fellowship, G.E.-M. an NSERC postdoctoral fellowship, E.V.D. the Danish Council for Independent Research (DFF-4181-00416), and C.L.G. a Royal Society fellowship. **Author contributions:** D.A.G., G.E.-M., C.L.G., and M.A. conceived the experiments. D.A.G., G.E.-M., C.L., and D.M.J. acquired and analyzed data. D.A.G., G.E.-M., and E.V.D. developed the theory and performed simulations. E.C. and M.H. grew the sample. D.A.G., G.E.-M., E.V.D., J.H.B., D.M.J., C.L.G., and M.A. prepared the manuscript. **Competing interests:** None declared. **Data and materials availability:** All data needed to evaluate the conclusions in the paper are present in the paper or the supplementary materials.

SUPPLEMENTARY MATERIALS

www.sciencemag.org/content/364/6435/62/suppl/DC1
Supplementary Text
Figs. S1 to S8
Tables S1 and S2
References (*37*–*51*)

6 December 2018; accepted 8 February 2019
Published online 21 February 2019
10.1126/science.aaw2906

Science

Quantum interface of an electron and a nuclear ensemble

D. A. Gangloff, G. Éthier-Majcher, C. Lang, E. V. Denning, J. H. Bodey, D. M. Jackson, E. Clarke, M. Hugues, C. Le Gall and M. Atatüre

Science **364** (6435), 62-66.
DOI: 10.1126/science.aaw2906originally published online February 21, 2019

An exercise in spin control

Semiconductor quantum dots offer the highest rate and quality of single photons among all other solid-state quantum light sources. However, they lack access to a long-lived quantum memory, such as a proximal nuclear spin, that would make them competitive for large-scale quantum architectures. Gangloff *et al.* used the spin of a single electron and light to cool an ensemble of about 30,000 nuclei within semiconductor quantum dots (see the Perspective by Bayer). They then extended this approach to manipulate individual nuclear spins. The ability to manipulate the ensemble of nuclei coherently, down to the single nuclear spin, could lead to the realization of a quantum dot network where each node has its own dedicated quantum memory.

Science, this issue p. 62; see also p. 30

Science (print ISSN 0036-8075; online ISSN 1095-9203) is published by the American Association for the Advancement of Science, 1200 New York Avenue NW, Washington, DC 20005. The title *Science* is a registered trademark of AAAS.